

Impact of Reservoir Permeability, Permeability Anisotropy and Designed Injection Rate on CO₂ Gas Behavior in the Shallow Saline Aquifer at the CaMI Field Research Station, Brooks, Alberta

Yu, X., Ahmadinia, M., Shariatipour, S. M., Lawton, D., Osadetz, K. & Saeedfar, A.

Author post-print (accepted) deposited by Coventry University's Repository

Original citation & hyperlink:

Yu, X, Ahmadinia, M, Shariatipour, SM, Lawton, D, Osadetz, K & Saeedfar, A 2020, 'Impact of Reservoir Permeability, Permeability Anisotropy and Designed Injection Rate on CO₂ Gas Behavior in the Shallow Saline Aquifer at the CaMI Field Research Station, Brooks, Alberta', *Natural Resources Research*, vol. 29, no. 4, pp. 2735–2752.

<https://doi.org/10.1007/s11053-019-09604-3>

DOI 10.1007/s11053-019-09604-3

ISSN 1520-7439

ESSN 1573-8981

Publisher: Springer

The final publication is available at Springer via <http://dx.doi.org/10.1007/s11053-019-09604-3>

Copyright © and Moral Rights are retained by the author(s) and/ or other copyright owners. A copy can be downloaded for personal non-commercial research or study, without prior permission or charge. This item cannot be reproduced or quoted extensively from without first obtaining permission in writing from the copyright holder(s). The content must not be changed in any way or sold commercially in any format or medium without the formal permission of the copyright holders.

This document is the author's post-print version, incorporating any revisions agreed during the peer-review process. Some differences between the published version and this version may remain and you are advised to consult the published version if you wish to cite from it.

1 **Impact of reservoir permeability, permeability anisotropy and**
2 **designed injection rate on CO₂ gas behaviour in the shallow saline**
3 **aquifer at the CaMI Field Research Station, Brooks, Alberta**

4 **Xinran Yu¹, Masoud Ahmadinia^{2,*}, Seyed M. Shariatipour², Don Lawton^{1,3}, Kirk**
5 **Osadetz³ and Amin Saeedfar³**

6
7 ¹ University of Calgary, Calgary, CANADA

8 ² Centre for Fluid and Complex Systems, Coventry University, UK

9 ³ Containment and Monitoring Institute, Calgary, CANADA

10
11
12 *Correspondence: Ahmadinm@uni.coventry.ac.uk

13
14 **Abstract**

15 Carbon capture and storage (CCS) is part of Canada's climate change action plan to
16 reduce greenhouse gas (GHG) emissions. The Containment and Monitoring Institute
17 Field Research Station (FRS) contributes to scientific and technological progress that
18 ensures the secure underground storage of CO₂. In this study, the process of shallow
19 CO₂ gas injection (300 m) and subsequent plume development at the FRS is
20 investigated using numerical simulation. Due to reservoir uncertainties, various
21 sensitivity analyses are performed to illustrate their effects on CO₂ saturation, plume
22 distribution and CO₂ dissolution in a saline reservoir in response to variations in
23 horizontal permeability (k_h), k_v/k_h ratio and CO₂ injection rate. The distance of
24 horizontal migration of the plume post-injection is predicted analytically and the result
25 is validated against the numerical simulation prediction.

26 Results show that increases in k_v/k_h ratio result in increases in both vertical and lateral
27 plume migration and decreases in dissolution rate and CO₂ solubility. It is also indicated
28 that the subsequent post-injection CO₂ migration rate is independent of both k_v/k_h and
29 previous injection rate. Dissolution varies significantly with changes in horizontal
30 permeability. The model shows that increased horizontal permeability facilitates plume
31 migration vertically and horizontally. Modeled permeability variations in horizontal
32 permeability (k_h), k_v/k_h ratio have a progressively decreasing effect on plume vertical
33 migration with time, while lateral migration effects increase with time.

34 **Keywords:** Case Study; Carbon Capture and Storage; CaMI Field Research Station;
35 k_v/k_h ratio.

36 **1. Introduction**

37 Carbon Capture and Storage (CCS) plays an important role in mitigating climate
38 change, as it provides a means of capturing and safely storing carbon from industrial
39 emissions in subsurface geological media (UNCCS 2015). Both capture and storage in
40 geological media must be performed efficiently to minimize CCS economic costs and
41 energy requirements. Storage in geological media must be safe and secure to ensure
42 public acceptance and safety and avoid contamination of other resources such as
43 potable groundwater (IEA 2013). Currently, CCS is focused strongly on pore space
44 storage in geological formations, predominately sandstones, due to their apparent lower
45 economic costs and energetics (Metz 2005).

46 Subsequent to injection, the sequestered free CO₂ phase has the potential to migrate
47 upwards due to buoyancy (a result of its low density) or to be influenced by
48 hydrogeological mechanisms, such as regional formation water flow (Juanes et al.
49 2010). Buoyant motions are inhibited by storage complex cap rock lithological and
50 permeability characteristics, while lateral migration is inhibited by lateral permeability
51 variations due to storage complex structure and rock body stratification, in ways
52 identical to petroleum entrapment, which is effective on timescales approaching 100
53 million years. However, storage complex containment risks are all positive and finite,
54 due to uncertainties in both storage complex geological characterization and
55 geomechanical changes induced, more likely during injection interval, but persisting
56 into the post-injection interval. The security of the storage process is a priority that
57 cannot be assured by its pre-injection characterization, that must be assured by
58 continuous monitoring both during and subsequent to the injection interval (Bachu
59 2008; Carroll et al. 2009; Morris et al. 2011; Rutqvist et al. 2007). To avoid CO₂
60 escaping the storage complex site, the plume migration is of great importance to track
61 and assess during injection and post-injection intervals.

62 The potential effects of storage complex pressure changes, as a function of storage
63 complex permeability and porosity during and subsequent to the injection interval, can
64 limit both storage complex capacity and injection rate (Birkholzer et al. 2015). The
65 subsurface pressure effects extend beyond the physical limits of the plume of injected
66 fluid and, although pressure interference is typically not permitted, this can impact other
67 subsurface activities and wells – both withdrawals and introductions - typically, but not

68 exclusively, in the storage formation (Birkholzer and Zhou 2009). Therefore, storage
69 complex pressure management is critically significant for project regulatory
70 compliance. Additional subsurface interventions have been proposed to manage
71 subsurface pressure impacts while improving storage project performance such as,
72 brine production, both active or passive may improve project performance, increasing
73 both higher storage capacity and injectivity in the storage complex (Bergmo et al. 2011;
74 Birkholzer et al. 2012; Buscheck et al. 2012; Cihan et al. 2015; Dempsey et al. 2014).

75 Compliance with typical regulatory requirements for permission to inject and store in
76 subsurface pore space typically requires a model of the proposed injection program
77 performed in consideration of the geostatic model at the proposed storage complex site
78 (Tucker et al. 2016). In practice, it is necessary to monitor the project to demonstrate
79 the containment of the injected fluid in the storage complex. It is also important to show
80 that project performance conforms with the reservoir models for eventual project
81 regulatory approval, risk assessment and liability transfer (Rock et al. 2017). Some
82 monitoring technologies have been applied to the existing sites recently, such as 4D
83 seismic and 4D gravity, by which CO₂ saturation and migration plume are successfully
84 detected (Arts et al. 2004; Daley et al. 2007).

85 In addition to these monitoring technologies, some research work has been conducted
86 to investigate the impacts of some geological properties on the behaviour and vertical
87 and horizontal movement of CO₂ plume (Ahmadinia et al. 2019; Bryant et al. 2006;
88 Doughty 2010; Flett et al. 2007; Hesse and Woods 2010; Hovorka et al. 2004; B. Li
89 and Benson 2015; Shariatipour, Pickup, et al. 2016a, 2016b; Taku Ide et al. 2007; Zhou
90 et al. 2010). The influence of small-scale heterogeneities on upward CO₂ plume
91 migration is studied by Onoja and Shariatipour (2019) and B. Li and Benson (2015),
92 and they find that ignoring small-scale heterogeneities can result in an overestimation
93 of the migration speed. Sensitivity studies conducted by Doughty (2010) indicate that
94 some model parameters including permeability, permeability anisotropy and the
95 maximum residual gas saturation also strongly affect the extent of CO₂ plume
96 movement. Some scholars have also investigated the impact of the permeability
97 anisotropy (k_v/k_h) by using three k_v/k_h values (0.01, 0.1 & 1) and found out that k_v/k_h is
98 a very influential factor on plume migration and CO₂ dissolution during the CO₂
99 injection into the storage formations (Shariatipour, Mackay, et al. 2016). Additionally,

100 capillary pressure plays an important role in CO₂ migration (Onoja et al. 2019; Zhou et
101 al. 2010). Al-Khdheawi et al. (2017) demonstrate that reservoir wettability and
102 heterogeneity both have impacts on CO₂ plume migration: a higher CO₂ wettability in
103 the reservoirs helps with CO₂ vertical migration while a water-wet reservoir always
104 retains CO₂ movement; reservoir heterogeneity reduces the vertical migration and
105 induces the lateral migration. Previous simulation works presented by Chasset et al.
106 (2011) and Newell et al. (2019) show that stratigraphic uncertainty is also an important
107 factor of the upward progression of the injected CO₂. Therefore, it is significant to
108 characterize the reservoir properties and constrain these parameters prior to CO₂
109 injection (Doughty 2010).

110 The FRS is designed primarily as a facility to demonstrate and develop monitoring
111 technologies (Lawton et al. 2019). It attempts to identify a simulated containment
112 failure in the hypothetical underlying storage complex, while ensuring the protection of
113 the groundwater and surficial resources, facilities and environments (<225 m to
114 surface). While shallow formations are not typically considered as efficient storage CO₂
115 sequestration reservoirs due to the low density of gas phase storage (Yang et al. 2014),
116 they are commonly available and they might provide economical storage options,
117 especially where low ground temperatures provide the opportunity for conversion to a
118 methane clathrate, as in the Athabasca region of Alberta, or sub-permafrost settings
119 (Zatsepina et al. 2014). As CO₂ is injected into a depleted methane reservoir, reservoir
120 pressure initially rises to meet conditions for hydrate formation. As hydrate forms, the
121 reservoir temperature increases following the equilibrium of the three-phase hydrate
122 equilibrium. CO₂ fraction in the hydrate phase rises with injection time and methane
123 can be displaced by injected CO₂ (Zatsepina et al. 2014).

124 **1.1 Objective and Approach**

125 The objective of this study is to model a potential CO₂ injection and plume development
126 in a shallow saline aquifer in Upper Cretaceous sandstones at the FRS and to improve
127 the characterization and understanding of CO₂ migration in a shallow formation, where
128 gas-phase CO₂ interacts with pore space fluids as it moves away from the point of
129 injection. The results of this study can be used to compare the actual plume migration
130 in the storage site in the future during the injection phase and/or when surface and
131 downhole monitoring data are available.

132 Various sensitivity analyses are performed to illustrate their impacts on CO₂ saturation,
133 plume distribution and CO₂ dissolution using different horizontal permeability values,
134 k_v/k_h ratio, and injection rate. Horizontal migration distance at the end of injection is
135 calculated using numerical models and analytical methods and the results of both are
136 compared. We also investigate the impact of caprock structure by comparing model
137 plume migration in a layer-cake reservoir model compared to the actual structural
138 reservoir model. In addition to evaluating monitoring technologies that can detect
139 potential containment loss from a deep CO₂ storage complex into a shallow saline
140 aquifer (300 m), the future comparison of our simulation outputs against the FRS
141 monitoring and verification data will provide an improved understanding of injected
142 gas migration processes and pathways in the shallow subsurface.

143 Although the FRS project looks primarily at the containment and monitoring of CO₂
144 storage especially from the perspective of monitoring, this ensures and detects threats
145 to both the groundwater protection zone and surface environments. Additionally, the
146 FRS provides us with an opportunity to consider gas-phase CO₂ storage and plume
147 migration in a shallow saline aquifer, which may inform some novel CO₂ storage
148 opportunities, such as shallow Athabasca region storage as a gas hydrate.

149

150 **2. Methodology**

151 **2.1 Description of FRS**

152 The FRS is located approximately 25 km southwest of Brooks, Alberta Canada (Figure
153 1), which is located on 200 hectares where both the surface and subsurface land are
154 owned privately by Torxen Energy (Lawton et al. 2017).

155 The CO₂ injection well may operate at a rate of up to 1,000 tonnes per year (t/yr.). The
156 injection experiment is designed to test the detection threshold of a variety of
157 monitoring technologies (Lawton et al. 2017, 2019), but the consequential CO₂
158 injection program results in shallow pore space storage that is amenable to the analysis
159 presented below. The shallow (~300 m) storage reservoir occurs in the Belly River
160 Group, Oldman Formation basal shoreface sandstone. The injected CO₂ plume
161 migration and pore water CO₂ concentration will be monitored, and its containment will
162 be studied with an array of geophysical and geochemical monitoring tools deployed
163 within three wells that penetrate the injection zone, as well with additional shallow

164 geophysical technologies, water wells (<150 m deep) and approximately five dozen soil
165 gas monitoring stations (Lawton et al. 2019). The Geo-model for this study is provided
166 by CMC Research Institutes Inc (Lawton et al. 2017).

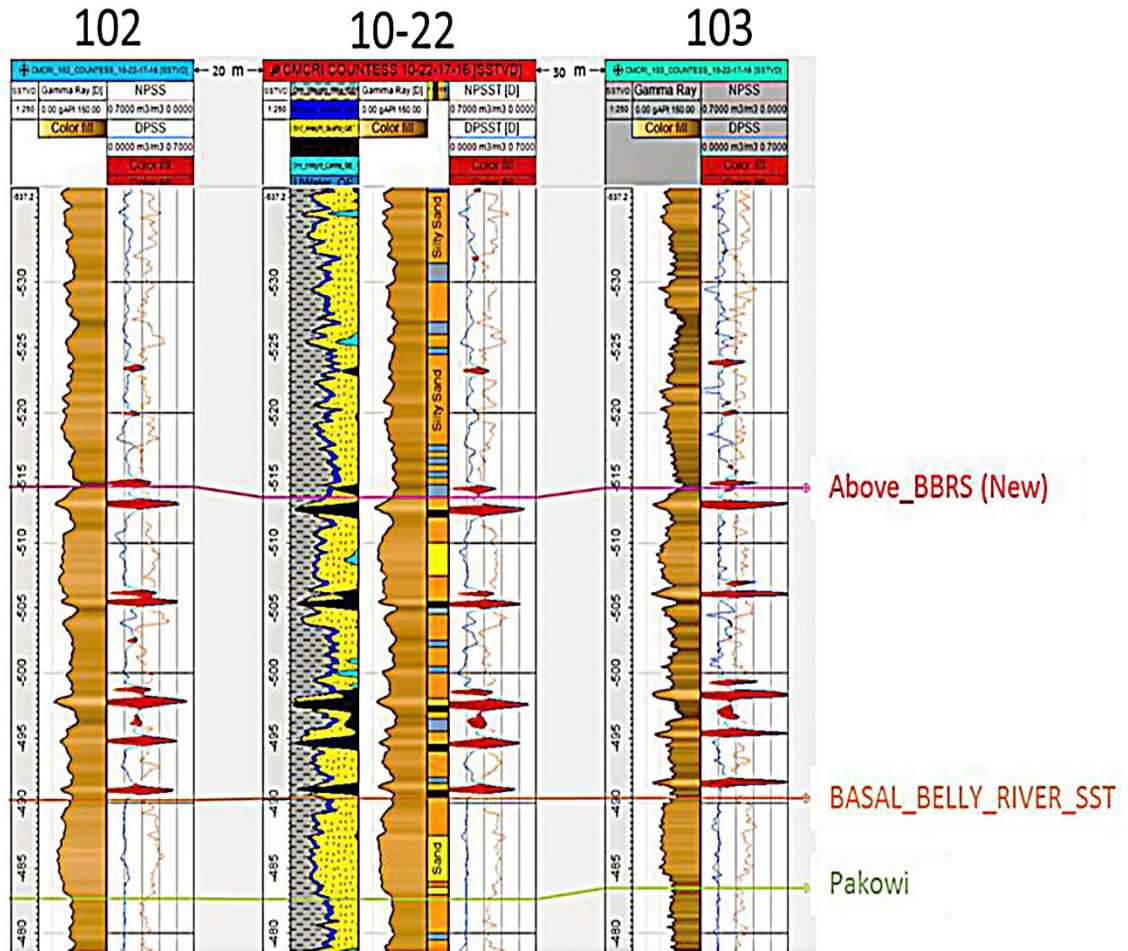


167
168

Figure 1. Location of the FRS.

169 **2.2 Description of the geological model**

170 Three vertical wells were drilled at the FRS (Lawton et al. 2017; Macquet et al. 2019).
171 The injection well was drilled to 550 mKB (metres below Kelly Bushing) TD, through
172 a succession of Upper Cretaceous strata that includes, in ascending stratigraphic order,
173 Upper Colorado Group (predominantly shale with lesser sandstone (Medicine Hat
174 Formation)), Lea Park Formation (predominantly siltstone and shale, with a few fine
175 sandstones near the top), and Belly River Group (predominantly sandstones, siltstones,
176 mudstones and coals). The wireline log interpretations from the three FRS wells are
177 shown in Figure 2 (Lawton et al. 2017). The injection well is “plugged back” and
178 completed to inject CO₂ into shoreface sandstones at the base of Belly River Gp. at
179 about 300 mKB, which is the approximate TD of the two deepest monitoring wells
180 (Figure 2) (Lawton et al. 2017; Macquet et al. 2019).



181

182

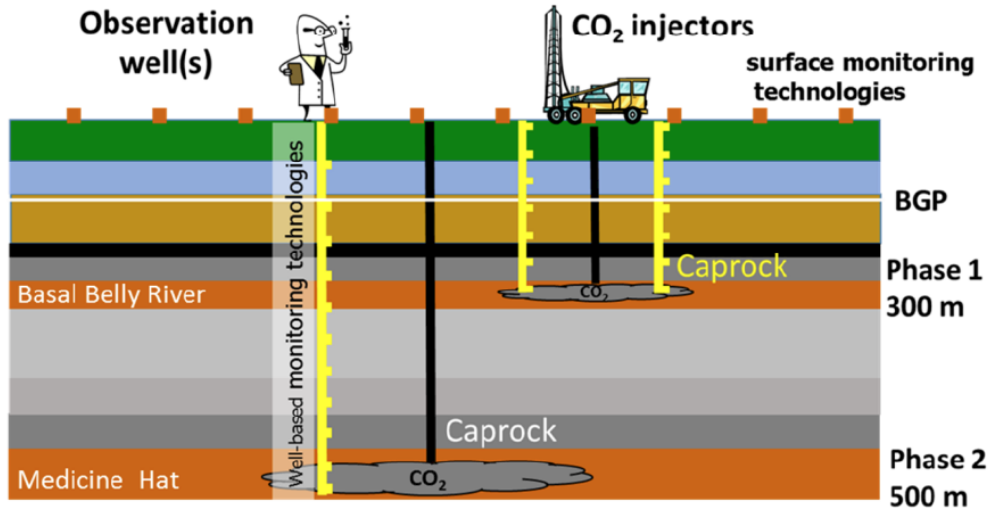
183 **Figure 2.** Interpretation of well logs from FRS. Well 102 is a geophysical observation well. Well 10-22
 184 is the injection well and well 103 is a geochemical observation well (Lawton et al. 2017).

185 Additional details on the geological setting are discussed by Lawton et al. (2017).

186 Currently injection occurs only into the basal Belly River sandstone at 300 mKB (Phase

187 1), although there is future potential to inject into the Medicine Hat Formation at 500

188 mKB (Phase 2) (Figure 3).



189

190 **Figure 3.** Schematic depth section of the Field Research Station (Phase 1: 300m, Phase 2: 500m)
 191 (Lawton et al. 2017).

192 The injection zone is predominantly saline water-saturated sandstones overlain by
 193 caprock shales and mixed sand/coal/shale successions (Lawton et al. 2017). In our
 194 simulation, the CO₂ injection rate is a constant 1,000 t/yr. for five years, with a
 195 cumulative 5000 t of CO₂ injected. The CO2STORE routine in Eclipse software is used
 196 for the simulation. Redlich-Kwong (RK) equation of state provides fluid properties.
 197 The solubility is calculated using previous work (Chang et al. 1996). The effect of salt
 198 and CO₂ on the water density is calculated using Ezrokhi's method (Zakirov et al.
 199 2014).

200 Key reservoir model properties are listed in Table 1 (Dongas and Lawton 2016).

201

Table 1. Key reservoir properties at the FRS

Parameter	Value
Reservoir Dimensions (NX×NY×NZ)	124×124×73
Refined section Dimensions (NX×NY×NZ)	224×224×18
Cell size (X & Y) (m)	8
Total number of 3D grid cells	1122448
Rock compressibility (1/bars)	4.18 e-4
Porosity (mean) (%)	11
Permeability (mean) (mD)	0.57
Viscosity of water (Pa.s)	1.205 e-3
Viscosity of CO ₂ (Pa.s)	1.49 e-5
Density of water (kg/m ³)	1000.74

Density of CO ₂ (kg/m ³)	68.02
CO ₂ -water relative permeability	S _w =0.5, k _{rCO₂} =0.5 k _{rwater} =0.00121
Salinity (ppm)	1000
<i>k_v/k_h</i> (base case)	0.1
Pressure at the 300 m depth (MPa)	2.944
Reservoir temperature (isothermal) (°C)	20
Annual Uniform Injection Rate (t/yr)	1,000
Base Case Injection Interval (yr.)	5
Simulation period (yr.)	15

202

203 Relative gas-water permeability curves are calculated using the widely accepted model
204 based on capillary pressure data (K. Li and Horne 2006). The CO₂-water relative
205 permeability end-point is calculated using the Brooks-Corey approximation (Brooks
206 and Corey 1964). Figure 4 shows the model input relative permeability curves. The
207 minimum water saturation and critical water saturation are set at 0.5. The maximum
208 water saturation and the corresponding water relative permeability are set at 1. Except
209 for CO₂ dissolution into water, geochemical compositional or phase changes are not
210 considered, the maximum allowable BHP is 6.615 MPa, which is 90% of the calculated
211 lithostatic pressure at the datum depth (300 mKB). In addition, some vertical and
212 horizontal fractures are indicated from core measurements, but these are not included
213 in the modeling. Remaining model uncertainties include reservoir pressure, fracture
214 pressure, capillary pressure, vertical to horizontal permeability ratio, horizontal
215 permeability and gas-water relative permeability. Additional model details are available
216 (Dongas and Lawton 2016).

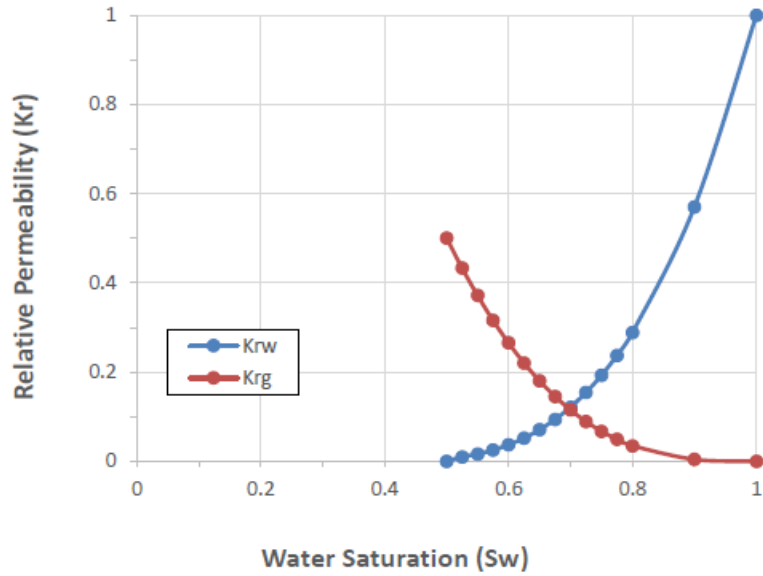


Figure 4. Relative permeability curve of CO₂/water (Dongas and Lawton 2016).

2.3 Sensitivity analysis set-up

We perform a sensitivity analysis to evaluate the impact of variations in horizontal permeability (k_h), vertical to horizontal permeability ratio (k_v/k_h), and injection rate on CO₂ saturation, the plume shape, and CO₂ dissolution. A few vertical and horizontal fractures are reported in the core analysis, most of them induced by the subsampling process and few of them observed in fresh slabbed cores, however, the presence of natural fractures cannot be precluded. At least three kilometres of sediments have been eroded since probably Mid-Eocene time, causing isostatic motions accompanying glacial loading and inter-glacial unloading. Although fracturing is not considered important, the variation in horizontal permeability and k_v/k_h can act as a rough attempt to simulate natural fractures, should they be present. Multipliers for injection rate are selected based on the regulation that BHP during injection does not exceed maximum allowable pressure that is a fraction of the lithostatic pressure. Different model scenarios are defined as shown in Table 2. For cases 2 and 3, vertical permeability is increased while horizontal permeability is kept constant. In cases 6 and 7, the injection period is decreased in correspondence to the rate, so the total injected CO₂ is the same as the base case. The modeled impacts of the caprock structure are also investigated by comparing the plume migration in the layered cake model to the observed structural model.

Table 2. Description of cases in the sensitivity analysis

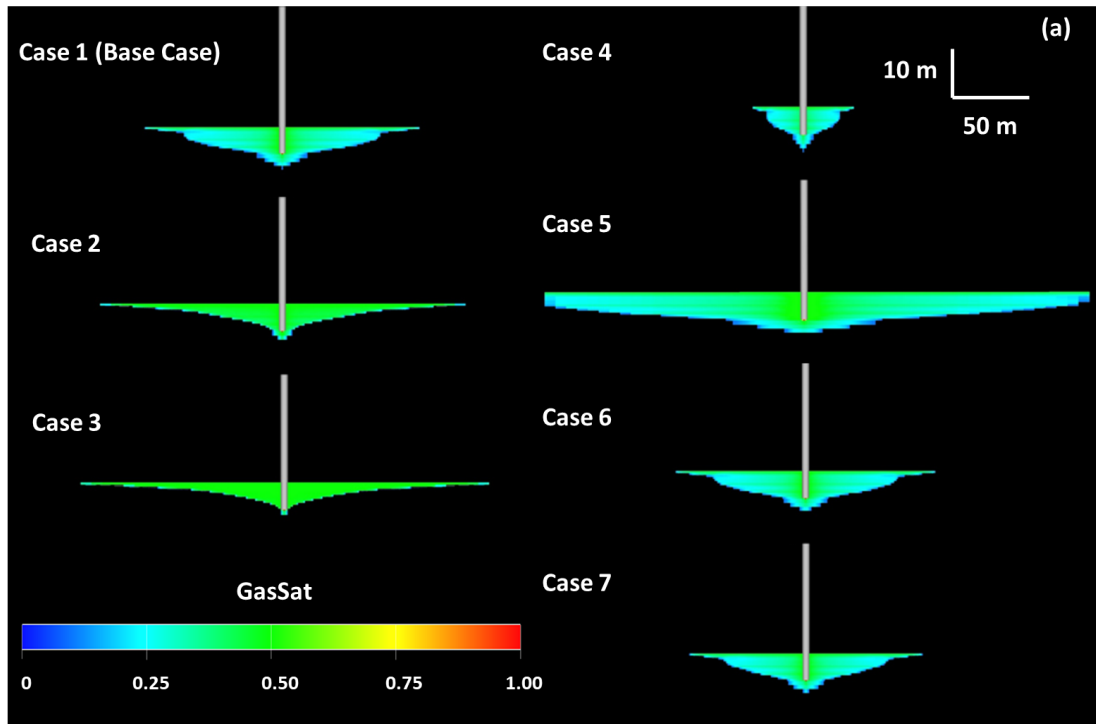
Case #	Description
1	Base case, see Table 1.
2	As per Table 1 except, $k_v/k_h \times 5$
3	As per Table 1 except, $k_v/k_h \times 10$
4	As per Table 1 except, $k_h \times 0.1$
5	As per Table 1 except, $k_h \times 10$
6	As per Table 1 except, injection rate $\times 1.2$ base case
7	As per Table 1 except, injection rate $\times 1.5$ base case

246 **2.4 Analytical solutions to migration distance**

247 We employ an analytical method proposed by Nordbotten et al. (2005) to calculate
 248 plume migration distances from the injection well. This approach is only valid during
 249 the injection phase, during time intervals equivalent to the first five years of our
 250 numerical models. The analytical results are then compared to those of both
 251 homogeneous and heterogeneous reservoirs from numerical simulations. More details
 252 of how to calculate the CO₂ plume analytical solution can be found in Appendix.

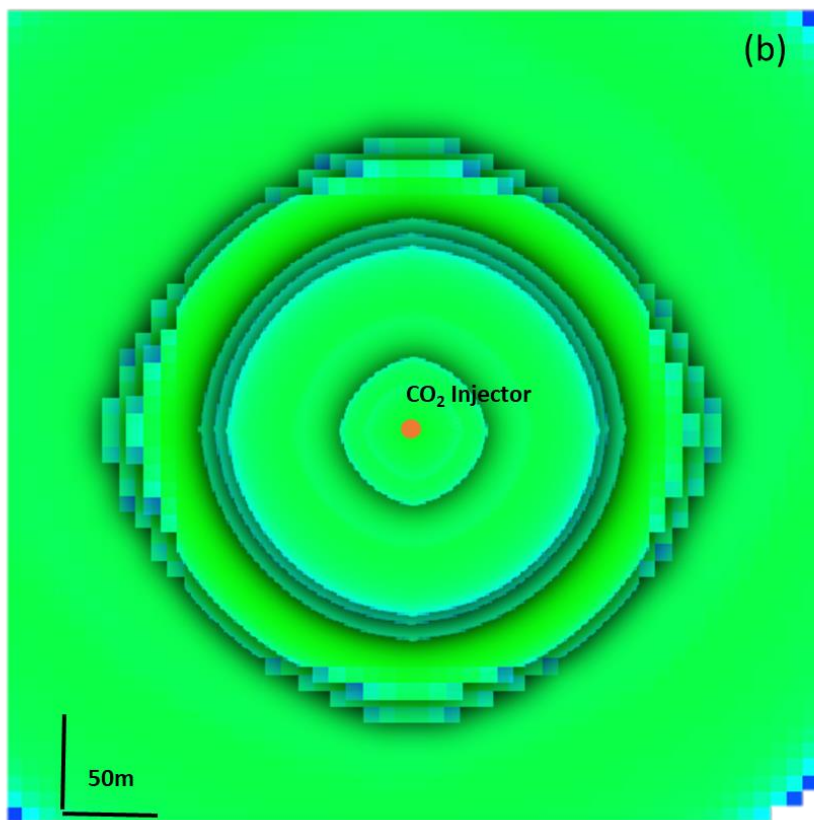
253 **3. Results and discussion**

254 The saturation distributions and plume boundary at the end of the simulation for all the
 255 cases are shown in figures 5 (a) and 5 (b), respectively. Figure 5 (a) shows that
 256 increasing vertical permeability (cases 2 and 3) results in a thinner plume, which is due
 257 to the comparative ease of upward migration intrinsic to this model. Models show
 258 horizontal permeability has a major impact on the plume extent, as the CO₂ has
 259 migrated farthest and nethermost away from the injector, in cases 5 and 4, respectively.
 260 Compared to cases 2 and 3, the plume is thicker in case 5 than in the base case, which
 261 results in a better distribution of the plume throughout the aquifer, suggesting a higher
 262 dissolution rate. In addition, the results also show the migration distance is a weak
 263 function of the injection rate that is a consequence of model structure, specifically the
 264 limited injectivity due to low formation permeability combined with the fixed total
 265 injected volume for all the models (injection period is longer for cases with lower
 266 injection rates).



267

268



269

270 **Figure 5.** Stratigraphic distribution of various model CO₂ saturation in the injection zone pore space **(a)**
 271 and the horizontal extent of various model plume boundaries **(b)** at the end of the simulation (15 years).
 272 The horizontal limit of various model plume boundaries (Figure 5a) is shown for, sequentially cases 4
 273 (smallest extent) through 7, 6, 1, 2, 3 and 5 (largest extent).

274 A summary of CO₂ plume horizontal migration distance and CO₂ saturation in the top
 275 layer for cases 1-7, at three time steps (1 month, 5 years, and 15 years) is shown in
 276 Table 3, and more details are discussed in Section 3.2.

277 **Table 3.** CO₂ plume horizontal migration distance and CO₂ saturation in the top layer for cases 1-7, at
 278 three time steps (1 month, 5 years, and 15 years).

Case #	CO ₂ plume horizontal migration distance (m)			CO ₂ saturation in the top layer (%)		
	1 month	5 years	15 years	1 month	5 years	15 years
1	7	74	103	0.31	0.49	0.5
2	7	87	133	0.31	0.49	0.5
3	7	96	145	0.35	0.5	0.51
4	1	20	34	0.07	0.39	0.44
5	23	107	149	0.42	0.5	0.51
6	7	72	95	0.32	0.48	0.49
7	7	68	86	0.31	0.49	0.49

279 In these simulations, the observation wells are located within 20 (well 1) and 30 metres
 280 (well 2) from the injector, respectively. Table 4 shows the time, saturation and layer at
 281 which the plume reaches each observation well. The times in Table 4 are a function of
 282 simulation time steps (one month). The cell saturation at the arrival time is provided.
 283 For example, the plume arrival time is the same for the base case and case 3, but the
 284 CO₂ saturation that plume reaches at the first observation well is higher for case 3.

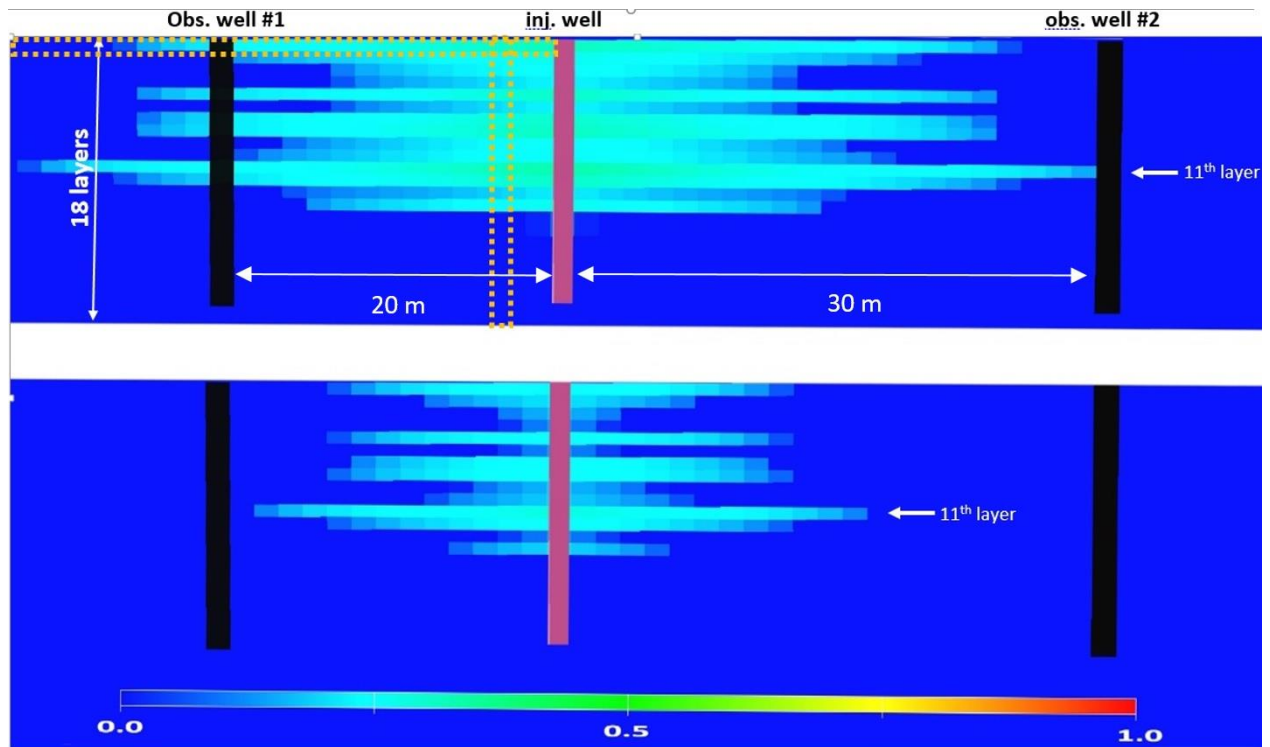
285 The model injected CO₂ plume reaches the closer observation well #1, located to the
 286 southwest of the injector, first. The model CO₂ plume arrives at the observation wells
 287 in less than 3 months in all model cases except Case 4, in which the plume takes about
 288 3 years to reach the observation well #1. In all cases, the CO₂ plume reaches observation
 289 wells first at model layer 11 but in cases 3 and 4, which have, respectively, the highest
 290 vertical permeability and lowest horizontal permeability the plume migrates to the
 291 observation well #2 first through model layer 1. In Case 3, this difference in the

292 migration pathway is due to the increased vertical permeability that results in the CO₂
 293 plume moving upwards faster compared to other models. In Case 3 most of the CO₂
 294 reaches the top, or first, layer through which it laterally, subsequently. In Case 4, the
 295 decreased horizontal permeability produces similar migration effects as the CO₂ tends
 296 to migrate upward until it is redirected horizontally after contacting the model caprock
 297 barrier. Changing the injection rate has no significant effect on plume migration during
 298 the first few months of injection (see also section 3.1.3, below) resulting in similar
 299 migration histories base case, and cases 6 and 7. This could be due to the low
 300 permeability that regardless of the rate, allows a certain amount of fluid flow.

301 **Table 4.** Time, saturation and layer at which CO₂ plume reaches the observation wells

Case #	1 st observation well (20 m)			2 nd observation well (30 m)		
	Time to observe (days)	Saturation	layer	Time to observe (days)	Saturation	layer
1	91	0.19	11	151	0.07	11
2	91	0.17	11	181	0.14	11
3	91	0.13	11	181	0.14	1
4	1091	0.21	11	1821	0.22	1
5	31	0.23	11	31	0.27	11
6	91	0.19	11	151	0.07	11
7	91	0.19	11	151	0.07	11

302 Figure 6 shows the moment when the model CO₂ plume reaches observation wells 1
 303 (6a) and 2 (6b). The results for horizontal and vertical migrations of the plume in all
 304 cases are discussed below. The horizontal migration distances of the CO₂ plume in the
 305 1st model layer (left side of the well) which has slightly lower horizontal permeability
 306 than layer 11, is monitored at the FRS injection project. Model layers where horizontal
 307 and vertical migration are physically monitored at the FRS are shown by the dashed
 308 lines (Figure 6(b)).



309

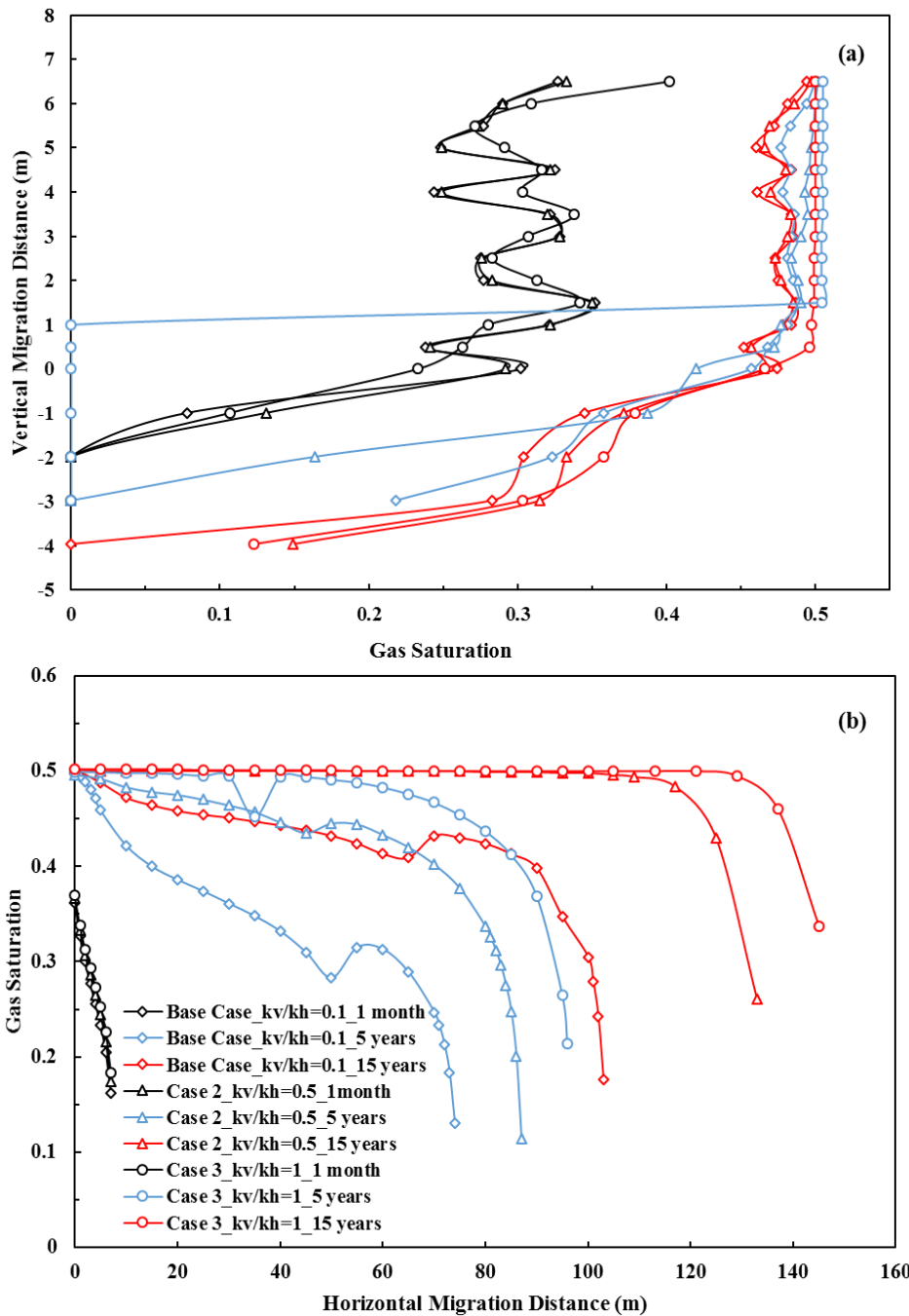
310 **Figure 6.** A cross-sectional view of CO₂ saturation distribution in the base case at the time of reaching
 311 observation wells #1(91 days after injection begins) and #2 (151 days after injection begins).

312 **3.1 CO₂ saturation distribution**

313 **3.1.1 Vertical to horizontal permeability ratio (k_v/k_h)**

314 The vertical to horizontal permeability ratio in the base case model is 0.1. This is
 315 increased to 0.5 and 1, in cases 2 and 3, respectively by increasing the vertical
 316 permeability only. In the base case, the CO₂ upwards migration is slower, which results
 317 in longer contact time with the pore space brine. Figure 7(a) shows CO₂ saturation along
 318 with the injectors versus vertical migration distance after one month, then five years
 319 and finally, 15 years for various (k_v/k_h) ratios of 0.1, 0.5 and 1, respectively. Vertical
 320 migration distance is defined by the distance between the top of the CO₂ plume and the
 321 lowest injection well perforation: zero-vertical migration coincides with the bottom of
 322 the perforations. As CO₂ migrates upwards, the vertical migration distance is positive
 323 and negative for portions of the plume below the lowest perforation. A small portion of
 324 the injected CO₂ migrates down to Pakowki Formation (below the Basal Belly River
 325 Group sandstone). One month after injection, the model CO₂ saturation distribution has
 326 a similar vertical trend in all three illustrated model cases (Figure 7). CO₂ also moves
 327 downward in cases 2 and 3 due to the higher k_v/k_h ratio. After five years, at the end of

328 injection, more CO₂ has accumulated in the upper model layers of the case 3 model as
 329 compared to the base case and case 2 models. After fifteen years, at the end of the
 330 simulation, the CO₂ saturation in upper model layers increases to 0.5 in case 3, when
 331 the saturation below the lowest perforation is zero, which illustrates the expected roles
 332 of vertical permeability and buoyant forces. In both the base case and case 2, which
 333 have lower model vertical permeability the injected CO₂ is calculated to be trapped in
 334 the bottom model layers between 6.5 m and 4.0 m below the lowest perforation.



335

336 **Figure 7.** CO₂ saturation versus vertical **(a)** and horizontal **(b)** migration distances at the time steps of
337 one month, five years, and 15 years, or the end of the simulation for model case 1-3 with various k_v/k_h
338 ratios as explained in the legend of the figure.

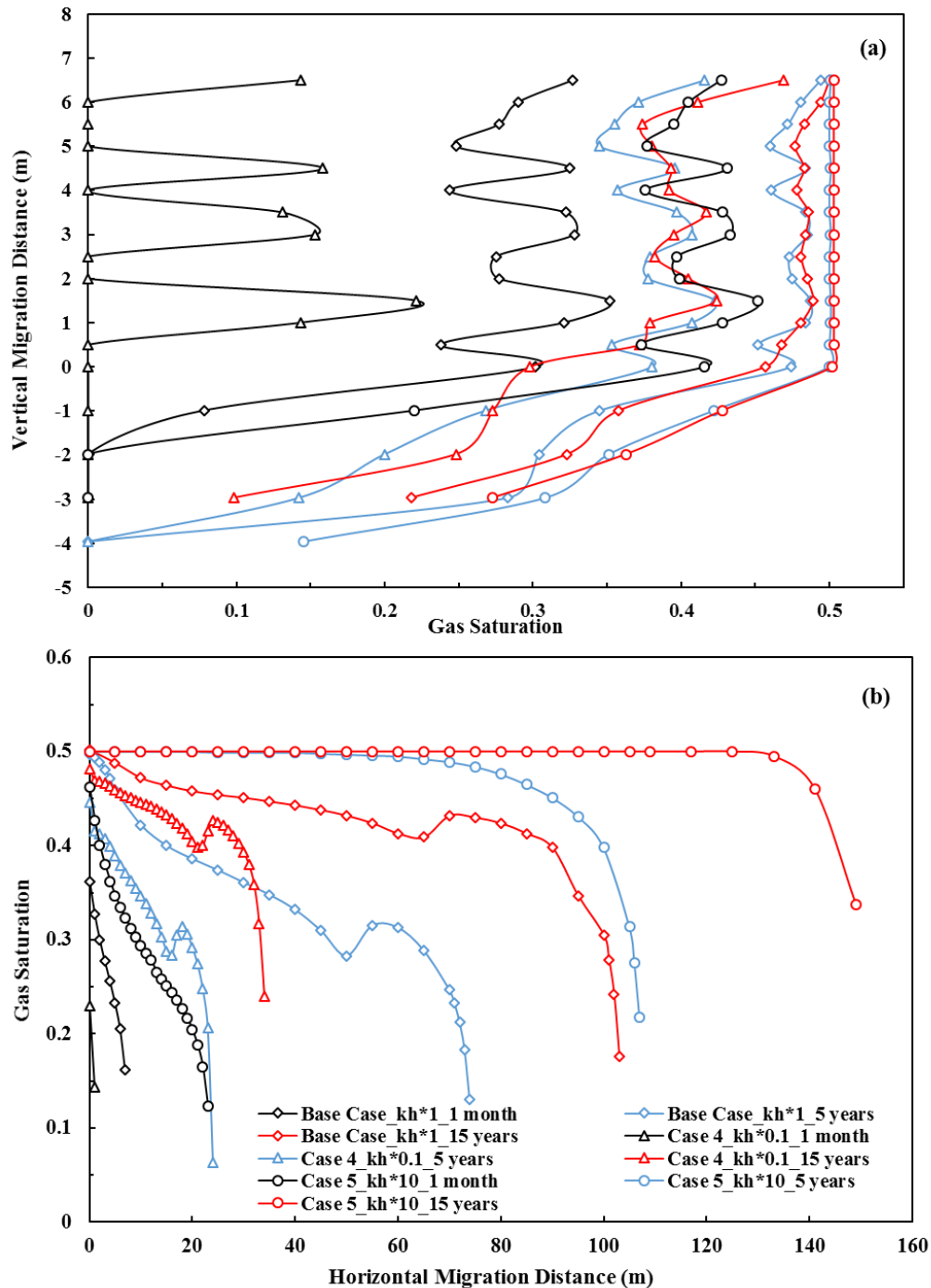
339 Figure 7(b) illustrates CO₂ saturation as a function of horizontal migration distance at
340 time steps of one month, five years and 15 years for (k_v/k_h) ratios of 0.1, 0.5 and 1. Zero
341 horizontal migration coincides with the injector well. After one month, the model CO₂
342 plume has migrated about 7 m laterally in all three illustrated model cases while after
343 five years, a higher k_v/k_h results in horizontal migration distances of 74 m, 87 m, and
344 96 m, for model cases 1-3 sequentially. Models predict that the CO₂ plume migrates
345 vertically more quickly as k_v/k_h , increases, such that it reaches the caprock earlier than
346 in model cases with lower k_v/k_h . In general, the sooner the plume contacts and is
347 deflected horizontally by the caprock the longer the horizontal migration time, and the
348 larger horizontal extent of the plume. The predicted lateral migration distance at the
349 end of the simulation is highest for model case 3 at 145 m, followed by 133 m for model
350 case 2 and smallest, or 103 m for the base case model.

351 The effect of k_v/k_h ratio on vertical and horizontal migration becomes more obviously
352 manifest with time, and the higher the k_v/k_h ratio the larger the vertical and horizontal
353 migration distances, typically. Moreover, higher k_v/k_h ratio models trap a larger
354 proportion of the injected CO₂ in stratigraphically higher model layers. Doughty (2010)
355 also finds that for a storage formation composed solely of sand, vertical anisotropy does
356 play a dominant role in controlling upward migration.

357 **3.1.2 Horizontal permeability**

358 Base case horizontal permeability is multiplied by factors of 0.1 and 10 in model cases
359 4 and 5, respectively. Model results show that horizontal permeability plays an
360 important role in vertical migration of the plume, as a result of the horizontal: vertical
361 permeability anisotropy (Figure 8a). In case 4, the lowest horizontal permeability case,
362 models predict that just a small portion of the injected CO₂ moved upwards and that its
363 downward migration is negligible a month after injection begins. CO₂ saturation in
364 upper model layers reached 0.3 and 0.4 in model cases 1 and 5, respectively. Except for
365 case 4, the model plume is predicted to migrate downward. Five years after injection
366 ends a small amount of CO₂ has migrated 4 m below the lowest perforation in all three
367 cases. At the same point in time, the CO₂ saturation in upper model layers has increased

368 to 0.36, 0.46 and 0.5 for cases 1, 4 and 5, respectively. A similar trend is predicted at
 369 the end of the simulation with slightly more CO₂ trapped in upper model layers (Figure
 370 8).



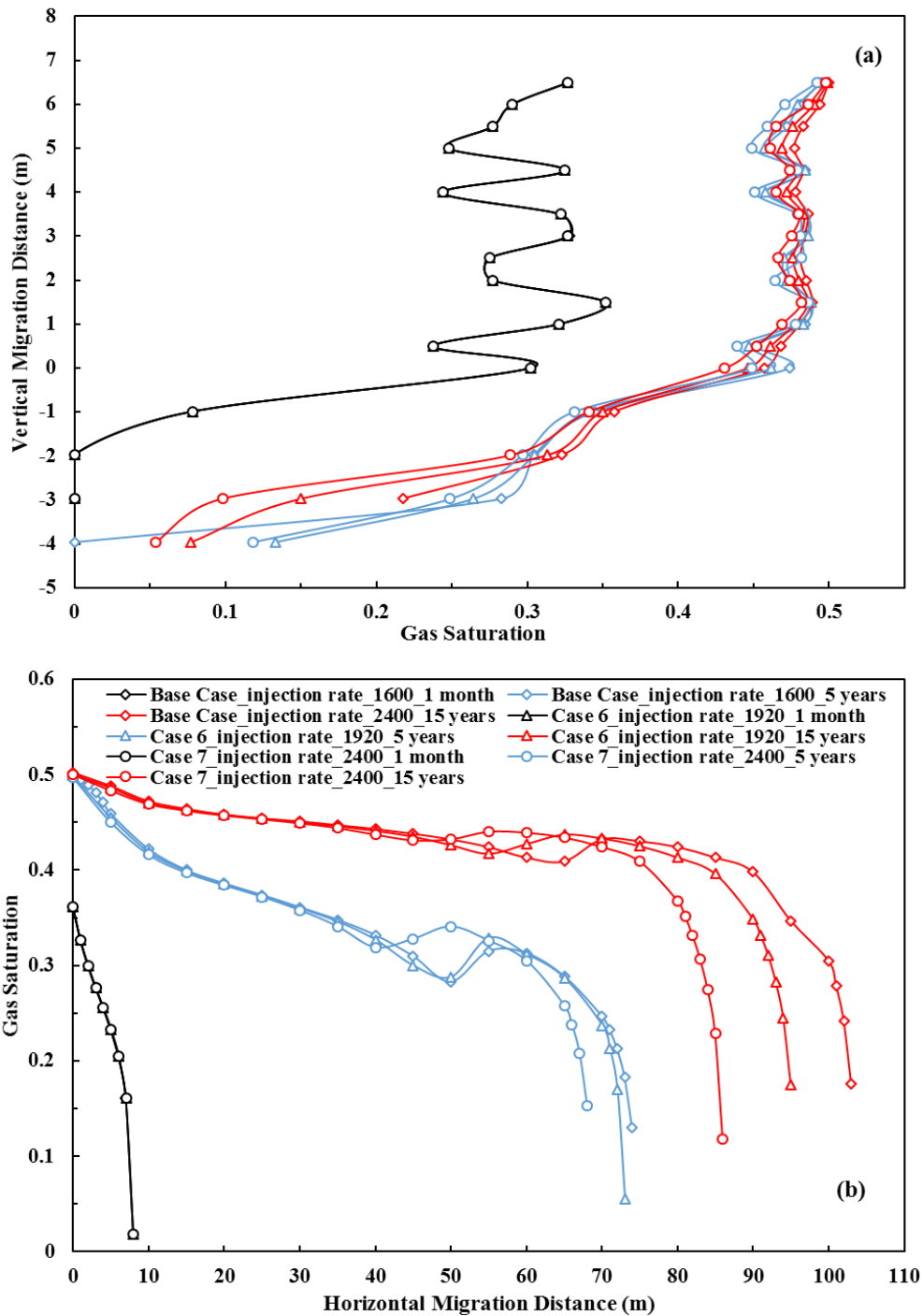
371
 372 **Figure 8.** CO₂ saturation versus vertical (a) and horizontal (b) migration distances at time steps of 1
 373 month, 5 years, and the end of the simulation (15 years), for three cases with different horizontal
 374 permeability.

375 Like the predicted vertical migration results, the horizontal migration distances are
376 larger with higher horizontal model permeability (Figure 8b). Following one month of
377 injection, the predicted horizontal migration distances are 1 m, 7 m, 23 m, for model
378 cases 4, 1 and 5, respectively. After 5 years, the case 5 migration result is 107 m but
379 only about 20 m for case 4, while in the base case the horizontal migration distance is
380 as discussed above. The horizontal plume extends 34 m, 103 m and 149 m for cases 4,
381 1 and 5, respectively, at the end of the simulation. The previous study also confirms
382 that higher horizontal permeability implies higher vertical permeability which enhances
383 model plume vertical migration with decreasing effectiveness as the model progresses
384 (Al-Khdheawi et al. 2017; Doughty 2010; Han et al. 2010).

385 **3.1.3 Injection rate**

386 Injection rates are specified in m^3/day at standard conditions. The base case injection
387 rate is $1600 \text{ sm}^3/\text{day}$, and this is increased by 20% to $1920 \text{ sm}^3/\text{day}$ and 50% to 2400
388 sm^3/day in model cases 6 and 7, respectively. The total injected volume is constant in
389 all model cases which implies shorter injection intervals for model cases 6 and 7. The
390 simulation results indicate vertical migration distance is a weak function of the injection
391 rate and that the plume's upward movement is similar for all model cases due to the
392 low vertical model permeability (Figure 9a).

393 In the first a few years, vertical and horizontal migration distances are, as a result,
394 similar for all model cases, which is probably a consequence of the small injected
395 volume and the resolution of the model. At the end of the simulation model, horizontal
396 plume migration distances are 103 m, 95 m, and 86 m in model cases 1, 6 and 7,
397 respectively. This suggests that injection at a lower rate over longer interval results in
398 a more even distribution in the reservoir for given total injected volume of CO_2 .
399 Therefore, the variation of injection rate is seen to influence horizontal migration more
400 strongly than vertical migration and that, for a given total injected volume, a lower
401 injection rate results in a smaller maximum horizontal plume development. This has
402 been reported by Yang et al. (2014) that the determination of an optimum injection rate
403 is necessary to avoid the CO_2 leakage and improve storage efficiency in a shallow saline
404 aquifer.



405

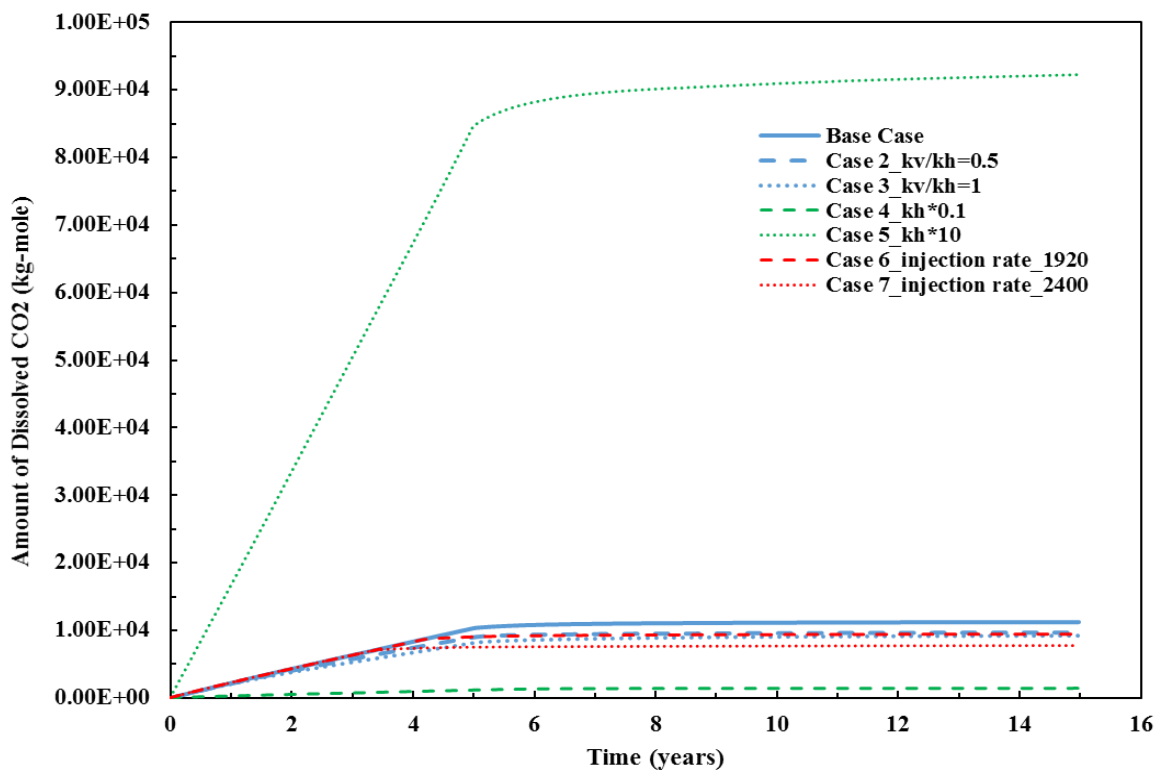
406 **Figure 9.** CO₂ saturation versus vertical (a) and horizontal (b) migration distances at the time steps of 1
 407 month, 5 years, and the end of the simulation (15 years) for three cases with different injection rates.

408 **3.2 Amount of CO₂ dissolved in brine**

409 **3.2.1 The k_v/k_h ratio**

410 A higher k_v/k_h ratio, such as in model cases 2 and 3, results in lower predicted CO₂
 411 dissolution. Figure 10 shows the cumulative amount of dissolved CO₂ in water (kg-

412 mole) for all seven cases. The cumulative dissolution increases during the five years
 413 over which CO₂ is injected. The graph shows a similar dissolution trend in the early
 414 injection period (first two years) for all model cases except 4 and 5 that represent the
 415 extreme variations of model horizontal permeability. This suggests that model
 416 dissolution is not significantly dependent on k_v/k_h variations among model cases 1, 2
 417 and 3. Subsequently, increased k_v/k_h ratios result in reduced model dissolution rates.
 418 During the post-injection period, the cumulative CO₂ dissolved in water is generally
 419 similar for model cases 1, 2 and 3, which are, respectively, 11 E+3, 9.65 E+3, and 9.15
 420 E+3 kg-mole. Above we saw that higher k_v/k_h ratio results in a predicted faster upwards
 421 migration and a thinner model plume of a larger horizontal extent. Therefore, a higher
 422 k_v/k_h ratio results in a lower dissolution rate and total dissolved CO₂ for reasons not
 423 immediately apparent.



424

425 **Figure 10.** The amount of CO₂ dissolved in water versus time is shown for all model cases.

426 **3.2.2 Horizontal permeability**

427 Although other parameters are seen to have little or no impact on CO₂ dissolution in
428 the early injection years, horizontal permeability significantly influences the rate and
429 amount of dissolved CO₂ throughout the injection period (model cases 4 and 5 in Figure
430 10). During injection, an increase or decrease in horizontal permeability results in
431 almost one order of magnitude increase or decrease in the amount of dissolved CO₂.
432 The total amount of dissolved CO₂ at the end of the simulation is around 9.1E+4,
433 1.1E+4 and 1.45E+3 kg-mole for model cases 5, 1 and 4, respectively. Moreover, while
434 the dissolution remains constant for most model cases during the post-injection period,
435 the results for case 5 predict a continuing increase rise that indicates the importance of
436 horizontal permeability for dissolution rate.

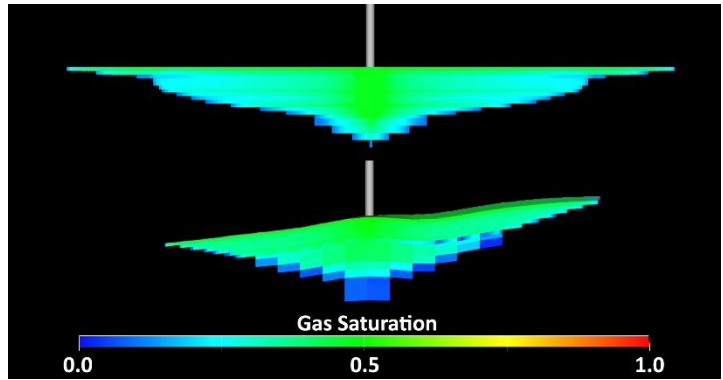
437 **3.2.3 Injection rate**

438 Because of the constant total amount of injected CO₂, the amount of model CO₂
439 dissolved in the pore water varies with the model injection rate. For case 6 (1920
440 sm³/day) the amount of dissolved CO₂ is 9440 kg-mole. However, the amount of
441 dissolved CO₂ decreases in models with a higher injection rate. The amount of
442 dissolved CO₂ is 7680 kg-mole for model case 7 (2400 sm³/day). During the injection
443 period, the total dissolved CO₂ is similar for model cases with similar permeability,
444 independent of the injection rate. This suggests that higher injection rates result in a
445 smaller plume that has less contact with fresh pore space brine (Figure 10).

446 **3.3. Effect of storage complex structure**

447 Storage complex structure especially that of the cap-rock, plays a significant role in
448 plume migration direction and trapping efficiency. Here, we compare a flat, layered
449 base case simulation (case 1) to a similar model that considers the real structural dip of
450 model strata. When the model structure is considered, the injected free gas moves
451 upwards below the caprock and much of the injected CO₂ becomes trapped in the small-
452 scale structural trap (Figure 11).

453

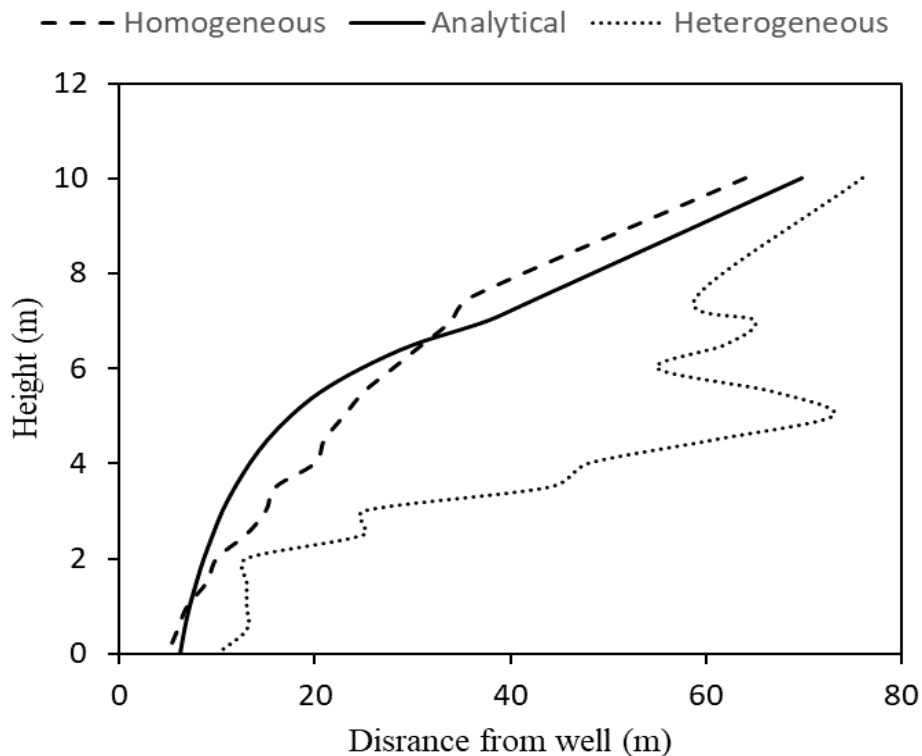


454
455

Figure 11. The effect of storage complex structure on injected CO₂ migration.

456 3.4 Comparison of analytical and numerical results

457 The base case horizontal migration distance is also calculated analytically (Nordbotten
458 et al. 2005), using the dimensionless parameter $\Gamma = 0.5$ as calculated using the injection
459 rate. These results are compared to base case horizontal migration distances from the
460 numerical simulation (Figure 12), except that the injection zone is made homogeneous
461 to more accurately resemble the analytical calculation.



462

463 **Figure 12.** Comparison of the migration distance for the analytical solution and homogenous and
464 heterogeneous numerical simulation at the FRS

465 The comparison shows that the results of the analytical solution are generally consistent
466 with the homogeneous and isotropic numerical model (Figure 12).

467 It can also be seen in Figure 12 that the migration plume obtained for the homogeneous
468 case is overall higher than that for the heterogeneous case. It is obvious that the reservoir
469 heterogeneity inhibits the vertical plume migration. However, the heterogeneity can
470 enhance the lateral movement, as is shown in Figure 12 that the horizontal migration
471 distance is 74 m in the heterogeneous model but only 62 m in the homogeneous model.
472 Overall, reservoir heterogeneity can also have an important influence on CO₂ plume
473 migration, which is also found by Al- Khdheewi et al. (2017).

474

475 **4. Conclusion**

476 The simulated CO₂ plume horizontal extent, vertical saturation distribution, and
477 dissolution rate at the FRS are studied by conducting a sensitivity analysis of selected
478 model parameters. The effects of variations in the k_v/k_h ratio, horizontal permeability,
479 and the injection rate are investigated. From the model results we conclude:

- 480 1. The effect of k_v/k_h ratios on vertical and horizontal migration is not apparent at
481 the start of injection but their effects become more significant with increasing
482 time. With a higher k_v/k_h ratio, both vertical and horizontal migration distances
483 increase. Higher model k_v/k_h ratios predict a lower dissolution rate and a lower
484 total amount of dissolved CO₂.
- 485 2. Higher horizontal permeability enhances the vertical migration rate initially,
486 although this effect declines over time. Models with high horizontal
487 permeability trap a proportion of injected CO₂ in the upper reservoir layers. CO₂
488 horizontal migration is facilitated by increased horizontal permeability. Models
489 outcomes with higher horizontal permeability also exhibit almost one order of
490 magnitude increased dissolved CO₂.
- 491 3. In all cases, the cumulative CO₂ injected is identical (i.e. the injection interval
492 is shorter for models with higher injection rates), vertical migration extent is
493 not dependent on injection rate, largely due to model architecture, but horizontal
494 migration is larger when injection rates are lower, probably due to a more even
495 distribution of CO₂ throughout the reservoir. Higher CO₂ injection rates are also

496 associated with slightly decreased model dissolution rates and decreased
497 cumulative dissolved CO₂.

498 4. Our results suggest that CCS project CO₂ injection rate should be carefully
499 determined considering the results of reservoir models.

500 5. The analytical analysis provides a useful method for confirming migration
501 distances obtained from numerical simulation, where an assumption of injection
502 zone homogeneity is reasonable.

503 6. The reservoir heterogeneity can enhance the lateral movement while inhibits the
504 vertical plume migration during the injection interval.

505

506 **5. Future work**

507 Although this study is based on the FRS, some conclusions are more generally
508 applicable to other CO₂ storage sites. Model sensitivity to the relative permeability
509 curve, capillary pressure merit further study. Having predicted the time of arrival and
510 shape of the plume at the FRS, the next step is to compare and analyze model
511 predictions against the observed arrival of injected CO₂ at the observation wells and the
512 various images of the plume when that occurs to better understand the conformance of
513 model and observed results.

514

515 **6. Acknowledgments**

516 The authors thank the Centre for Fluid and Complex Systems for the financial support of
517 this project. We thank the Containment and Monitoring Institute (CaMI) of CMC
518 Research Institutes Inc. for providing the geostatic model and petrophysical data for the
519 FRS. Research at the site is undertaken thanks in part to funding from the Canada First
520 Research Excellence Fund. Special thanks also to Dr. Phil Costen for reviewing the
521 paper and sharing his constructive comments.

522

523 **Appendix: Analytical solution of CO₂ plume**

524 The CO₂ plume analytical solution is Nordbotten et al. (2005)

$$525 \quad -\frac{\lambda-1}{r'((\lambda-1)b'+1)^2} + 2\Gamma r' b' + 2\Lambda r' = 0, \quad (1)$$

$$526 \quad \Lambda(\lambda-1)^2 - \Gamma\lambda \ln\left(\frac{\Gamma+\Lambda}{\Lambda\lambda}\right) = \frac{2\lambda[\Lambda(\lambda-1)-\Gamma]^2}{\lambda-1}. \quad (2)$$

527 where λ is the averaged phase mobility of water and CO₂, defined as $\lambda = \frac{b}{B}\lambda_c + \frac{B-b}{B}\lambda_w$,
528 and b denotes the thickness of the CO₂ layer, and B represents the total reservoir
529 thickness. $\lambda_\alpha = \frac{k_{r\alpha}}{\mu_\alpha}$, is the ratio of relative permeability to fluid viscosity, where α
530 represents each phase, with c for CO₂ and w for water. Λ denotes the Lagrangian
531 multiplier.

532 In addition, r' , b' and Γ are dimensionless variables, where $r' = r\sqrt{\frac{\pi B\phi}{Q_{well}t}}$, $b' = \frac{b}{B}$, and
533 $\Gamma = \frac{2\pi\Delta\rho g\lambda_w k B^2}{Q_{well}}$. In these equations, r denotes migration distance, $\Delta\rho$ is the density
534 differential between brine and CO₂, g is the gravitational constant, k is the average
535 permeability of the reservoir, ϕ is the average porosity, t is the injection period and
536 Q_{well} is the CO₂ injection rate. For simplicity, water and CO₂ viscosities and densities
537 are assumed constant. Fluid properties of CO₂ and brine used in these calculations are
538 shown in Table 1.

539

540 References

- 541 Ahmadiania, M., Shariatipour, S. M., Andersen, O., & Sadri, M. (2019). Benchmarking
542 of vertically integrated models for the study of the impact of caprock
543 morphology on CO₂ migration. *International Journal of Greenhouse Gas*
544 *Control*, 90(August), 102802. <https://doi.org/10.1016/j.ijggc.2019.102802>
- 545 Al-Khdheawi, E. A., Vialle, S., Barifcani, A., Sarmadivaleh, M., & Iglauer, S.
546 (2017). Impact of reservoir wettability and heterogeneity on CO₂-plume
547 migration and trapping capacity. *International Journal of Greenhouse Gas*
548 *Control*, 58, 142–158. <https://doi.org/10.1016/j.ijggc.2017.01.012>
- 549 Arts, R., Eiken, O., Chadwick, A., Zweigel, P., van der Meer, L., & Zinszner, B.
550 (2004). Monitoring of CO₂ injected at Sleipner using time-lapse seismic data.
551 *Energy*, 29(9–10), 1383–1392. <https://doi.org/10.1016/j.energy.2004.03.072>

- 552 Bachu, S. (2008). CO₂ storage in geological media: Role, means, status and barriers to
553 deployment. *Progress in Energy and Combustion Science*, 34(2), 254–273.
554 <https://doi.org/10.1016/j.pecs.2007.10.001>
- 555 Bergmo, P. E. S., Grimstad, A. A., & Lindeberg, E. (2011). Simultaneous CO₂
556 injection and water production to optimise aquifer storage capacity. *International*
557 *Journal of Greenhouse Gas Control*, 5(3), 555–564.
558 <https://doi.org/10.1016/j.ijggc.2010.09.002>
- 559 Birkholzer, J. T., Cihan, A., & Zhou, Q. (2012). Impact-driven pressure management
560 via targeted brine extraction-Conceptual studies of CO₂ storage in saline
561 formations. *International Journal of Greenhouse Gas Control*, 7, 168–180.
562 <https://doi.org/10.1016/j.ijggc.2012.01.001>
- 563 Birkholzer, J. T., Oldenburg, C. M., & Zhou, Q. (2015). CO₂ migration and pressure
564 evolution in deep saline aquifers. *International Journal of Greenhouse Gas*
565 *Control*, 40, 203–220. <https://doi.org/10.1016/j.ijggc.2015.03.022>
- 566 Birkholzer, J. T., & Zhou, Q. (2009). Basin-scale hydrogeologic impacts of CO₂
567 storage: Capacity and regulatory implications. *International Journal of*
568 *Greenhouse Gas Control*, 3(6), 745–756.
569 <https://doi.org/10.1016/j.ijggc.2009.07.002>
- 570 Brooks, R., & Corey, T. (1964). HYDRAU uc properties of porous media. *Hydrology*
571 *Papers, Colorado State University*, 24, 37.
- 572 Bryant, S. L., Lakshminarasimhan, S., & Pope, G. A. (2006). SPE 99938 Buoyancy -
573 Dominated Multiphase Flow and Its Impact on Geological Sequestration. *SPE*
574 *Journal*.
- 575 Buscheck, T. A., Sun, Y., Chen, M., Hao, Y., Wolery, T. J., Bourcier, W. L., et al.
576 (2012). Active CO₂ reservoir management for carbon storage: Analysis of
577 operational strategies to relieve pressure buildup and improve injectivity.
578 *International Journal of Greenhouse Gas Control*, 6, 230–245.
579 <https://doi.org/10.1016/j.ijggc.2011.11.007>
- 580 Carroll, S., Hao, Y., & Aines, R. (2009). Transport and detection of carbon dioxide in
581 dilute aquifers. *Energy Procedia*, 1(1), 2111–2118.
582 <https://doi.org/10.1016/j.egypro.2009.01.275>
- 583 Chang, Y.-B., Coats, B. K., & Nolen, J. S. (1996). A compositional model for CO₂
584 floods including CO₂ solubility in water. In *Permian Basin Oil and Gas*
585 *Recovery Conference*. Society of Petroleum Engineers.
- 586 Chasset, C., Jarsjö, J., Erlström, M., Cvetkovic, V., & Destouni, G. (2011). Scenario
587 simulations of CO₂ injection feasibility, plume migration and storage in a saline
588 aquifer, Scania, Sweden. *International Journal of Greenhouse Gas Control*, 5(5),
589 1303–1318. <https://doi.org/10.1016/j.ijggc.2011.06.003>
- 590 Cihan, A., Birkholzer, J. T., & Bianchi, M. (2015). Optimal well placement and brine
591 extraction for pressure management during CO₂ sequestration. *International*
592 *Journal of Greenhouse Gas Control*, 42, 175–187.

- 593 <https://doi.org/10.1016/j.ijggc.2015.07.025>
- 594 Daley, T. M., Solbau, R. D., Ajo-Franklin, J. B., & Benson, S. M. (2007). Continuous
595 crosswell monitoring of CO₂ injection in a brine aquifer. *Society of Exploration*
596 *Geophysicists - 77th SEG International Exposition and Annual Meeting, SEG*
597 *2007*, 72(5), 2949–2953. <https://doi.org/10.1190/1.2793083>
- 598 Dempsey, D., Kelkar, S., & Pawar, R. (2014). Passive injection: A strategy for
599 mitigating reservoir pressurization, induced seismicity and brine migration in
600 geologic CO₂ storage. *International Journal of Greenhouse Gas Control*, 28, 96–
601 113. <https://doi.org/10.1016/j.ijggc.2014.06.002>
- 602 Dongas, J. M., & Lawton, D. C. (2016). Static characterization and dynamic
603 simulated scenarios for monitoring a shallow CO₂ injection target, (Figure 1), 2–
604 6.
605 https://www.crewes.org/ForOurSponsors/ConferenceAbstracts/2016/CSEG/Dongas_CSEG_2016.pdf
606
- 607 Doughty, C. (2010). Investigation of CO₂ plume behavior for a large-scale pilot test of
608 geologic carbon storage in a saline formation. *Transport in Porous Media*, 82(1),
609 49–76. <https://doi.org/10.1007/s11242-009-9396-z>
- 610 Flett, M., Gurton, R., & Weir, G. (2007). Heterogeneous saline formations for carbon
611 dioxide disposal: Impact of varying heterogeneity on containment and trapping.
612 *Journal of Petroleum Science and Engineering*, 57(1–2), 106–118.
613 <https://doi.org/10.1016/j.petrol.2006.08.016>
- 614 Han, W. S., Lee, S.-Y., Lu, C., & McPherson, B. J. (2010). Effects of permeability on
615 CO₂ trapping mechanisms and buoyancy-driven CO₂ migration in saline
616 formations. *Water Resources Research*, 46(7), 1–20.
617 <https://doi.org/10.1029/2009wr007850>
- 618 Hesse, M. A., & Woods, A. W. (2010). Buoyant dispersal of CO₂ during geological
619 storage. *Geophysical Research Letters*, 37(1), 1–5.
620 <https://doi.org/10.1029/2009GL041128>
- 621 Hovorka, S. D., Doughty, C., Benson, S. M., Pruess, K., & Knox, P. R. (2004). The
622 impact of geological heterogeneity on CO₂ storage in brine formations: A case
623 study from the Texas Gulf Coast. *Geological Society Special Publication*, 233,
624 147–163. <https://doi.org/10.1144/GSL.SP.2004.233.01.10>
- 625 IEA. (2013). Technology Roadmap Carbon Capture and Storage–2013 Edition.
626 Organization for Economic Co-operation and Development/International Energy.
- 627 Juanes, R., MacMinn, C. W., & Szulczewski, M. L. (2010). The footprint of the CO₂
628 plume during carbon dioxide storage in saline aquifers: Storage efficiency for
629 capillary trapping at the basin scale. *Transport in Porous Media*, 82(1), 19–30.
630 <https://doi.org/10.1007/s11242-009-9420-3>
- 631 Lawton, D. C., Dongas, J., Osadetz, K., Saeedfar, A., & Macquet, M. (2019).
632 Development and analysis of a geostatic model for shallow CO₂ injection at the
633 Field Research Station, Southern Alberta, Canada. *Geophysics and*

- 634 *Geosequestration. Cambridge University Press, Cambridge, 280, 296.*
- 635 Lawton, D. C., Osadetz, K. G., & Saeedfar, A. (2017). CCS monitoring technology
636 innovation at the CaMI Field research station, Alberta, Canada. *EAGE/SEG*
637 *Research Workshop 2017 on Geophysical Monitoring of CO₂ Injections: CCS*
638 *and CO₂-EOR*, (Mmv), 5–9. <https://doi.org/10.3997/2214-4609.201701930>
- 639 Li, B., & Benson, S. M. (2015). Influence of small-scale heterogeneity on upward
640 CO₂ plume migration in storage aquifers. *Advances in Water Resources*, 83,
641 389–404. <https://doi.org/10.1016/j.advwatres.2015.07.010>
- 642 Li, K., & Horne, R. N. (2006). Comparison of methods to calculate relative
643 permeability from capillary pressure in consolidated water-wet porous media.
644 *Water Resources Research*, 42(6), 1–9. <https://doi.org/10.1029/2005WR004482>
- 645 Macquet, M., Lawton, D. C., Saeedfar, A., & Osadetz, K. G. (2019). A feasibility
646 study for detection thresholds of CO₂ at shallow depths at the CaMI Field
647 Research Station, Newell County, Alberta, Canada . *Petroleum Geoscience*, 25,
648 petgeo2018-135. <https://doi.org/10.1144/petgeo2018-135>
- 649 Metz, B. (2005). carbon dioxide capture and storage. *IPCC special report*, 342.
- 650 Morris, J. P., Detwiler, R. L., Friedmann, S. J., Vorobiev, O. Y., & Hao, Y. (2011).
651 The large-scale geomechanical and hydrogeological effects of multiple CO₂
652 injection sites on formation stability. *International Journal of Greenhouse Gas*
653 *Control*, 5(1), 69–74. <https://doi.org/10.1016/j.ijggc.2010.07.006>
- 654 Newell, A. J., Pourmalek, A., Butcher, A. S., & Shariatipour, S. M. (2019). The
655 importance of lithofacies control on fluid migration in heterogeneous aeolian
656 formations for geological CO₂ storage: Lessons from observational evidence and
657 modelling of bleached palaeoreservoirs at Salt Wash Graben, Utah. *International*
658 *Journal of Greenhouse Gas Control*, 91(September), 102841.
659 <https://doi.org/10.1016/j.ijggc.2019.102841>
- 660 Nordbotten, J. M., Celia, M. A., & Bachu, S. (2005). Injection and storage of CO₂ in
661 deep saline aquifers: Analytical solution for CO₂ plume evolution during
662 injection. *Transport in Porous Media*, 58(3), 339–360.
663 <https://doi.org/10.1007/s11242-004-0670-9>
- 664 Onoja, M. U., Ahmadinia, M., Shariatipour, S. M., & Wood, A. M. (2019).
665 Characterising the role of parametric functions in the van Genuchten empirical
666 model on CO₂ storage performance. *International Journal of Greenhouse Gas*
667 *Control*, 88(June), 233–250. <https://doi.org/10.1016/j.ijggc.2019.06.004>
- 668 Onoja, M. U., & Shariatipour, S. M. (2019). Assessing the impact of relative
669 permeability and capillary heterogeneity on Darcy flow modelling of CO₂
670 storage in Utsira Formation. *Greenhouse Gases: Science and Technology*,
671 26(2019), 1–26. <https://doi.org/10.1002/ghg.1932>
- 672 Rock, L., O'Brien, S., Tessarolo, S., Duer, J., Bacci, V. O., Hirst, B., et al. (2017).
673 The Quest CCS Project: 1st Year Review Post Start of Injection. *Energy*
674 *Procedia*, 114(November 2016), 5320–5328.

- 675 <https://doi.org/10.1016/j.egypro.2017.03.1654>
- 676 Rutqvist, J., Birkholzer, J., Cappa, F., & Tsang, C. F. (2007). Estimating maximum
677 sustainable injection pressure during geological sequestration of CO₂ using
678 coupled fluid flow and geomechanical fault-slip analysis. *Energy Conversion
679 and Management*, 48(6), 1798–1807.
680 <https://doi.org/10.1016/j.enconman.2007.01.021>
- 681 Shariatipour, S. M., Mackay, E. J., & Pickup, G. E. (2016). An engineering solution
682 for CO₂ injection in saline aquifers. *International Journal of Greenhouse Gas
683 Control*, 53, 98–105. <https://doi.org/10.1016/j.ijggc.2016.06.006>
- 684 Shariatipour, S. M., Pickup, G. E., & Mackay, E. J. (2016a). Investigation of CO₂
685 storage in a saline formation with an angular unconformity at the caprock
686 interface. *Petroleum Geoscience*, 22(2), 203–210.
687 <https://doi.org/10.1144/petgeo2015-039>
- 688 Shariatipour, S. M., Pickup, G. E., & Mackay, E. J. (2016b). Simulations of CO₂
689 storage in aquifer models with top surface morphology and transition zones.
690 *International Journal of Greenhouse Gas Control*, 54, 117–128.
691 <https://doi.org/10.1016/j.ijggc.2016.06.016>
- 692 Taku Ide, S., Jessen, K., & Orr, F. M. (2007). Storage of CO₂ in saline aquifers:
693 Effects of gravity, viscous, and capillary forces on amount and timing of
694 trapping. *International Journal of Greenhouse Gas Control*, 1(4), 481–491.
695 [https://doi.org/10.1016/S1750-5836\(07\)00091-6](https://doi.org/10.1016/S1750-5836(07)00091-6)
- 696 Tucker, O., Gray, L., Maas, W., Solutions, S. G., Brien, S. O., & Canada, S. (2016).
697 IPTC-18666-MS Quest Commercial Scale CCS – The First Year Overview of
698 the Quest CCS project, (November), 14–16.
- 699 UNCCS. (2015). Climate Action Now: Summary for Policymakers 2015.
- 700 Yang, F., Bai, B., Dunn-Norman, S., Nygaard, R., & Eckert, A. (2014). Factors
701 affecting CO₂ storage capacity and efficiency with water withdrawal in shallow
702 saline aquifers. *Environmental Earth Sciences*, 71(1), 267–275.
703 <https://doi.org/10.1007/s12665-013-2430-z>
- 704 Zakirov, I., I. Aanonsen, S., S. Zakirov, E., & M. Palatnik, B. (2014). Optimizing
705 Reservoir Performance by Automatic Allocation of Well Rates. *ECMOR V - 5th
706 European Conference on the Mathematics of Oil Recovery*, 375–384.
707 <https://doi.org/10.3997/2214-4609.201406895>
- 708 Zatsepina, O. Y., Hassanzadeh, H., & Pooladi-Darvish, M. (2014). Geological Storage
709 of CO₂ as Hydrate in a McMurray Depleted Gas Reservoir. *Gas Injection for
710 Disposal and Enhanced Recovery*, 9781118938(September), 311–329.
711 <https://doi.org/10.1002/9781118938607.ch18>
- 712 Zhou, Q., Birkholzer, J. T., Mehnert, E., Lin, Y. F., & Zhang, K. (2010). Modeling
713 basin- and plume-scale processes of CO₂ storage for full-scale deployment.
714 *Ground Water*, 48(4), 494–514. [https://doi.org/10.1111/j.1745-
715 6584.2009.00657.x](https://doi.org/10.1111/j.1745-6584.2009.00657.x)

